Observational Analysis of a Gust Front to Bore to Solitary Wave Transition within an Evolving Nocturnal Boundary Layer

KEVIN R. KNUPP

Department of Atmospheric Science, University of Alabama in Huntsville, Huntsville, Alabama

(Manuscript received 18 August 2005, in final form 14 December 2005)

ABSTRACT

The evolution of a gust front to bore to solitary wave transition, and comprehensive information on the evolving nocturnal boundary layer (NBL) associated with this change, are described with analysis of radar and profiler measurements. The observations were obtained on 21 June 2002 in the Oklahoma panhandle during the International H_2O Project. The evolution of this system, from a strong bore (initiated by a vigorous gust front) to a solitary wave, was observed over a 4-h period with Doppler radar and surface measurements. Detailed information on the mature bore structure was obtained by a cluster of profiling instruments including two boundary layer wind profilers, a lidar ceilometer, and a microwave profiling radiometer.

A strong bore was initiated by an extensive gust front that perturbed an incipient NBL whose development (prior to sunset) was enhanced by shading from the parent mesoscale convective system. At the time of bore formation, the NBL was about 300 m deep and exhibited a surface temperature about 4 K less than the afternoon maximum. Initially, the bore assumed kinematic properties similar to those of a gust front. As the NBL stabilized, the bore matured and exhibited undular formations over 30–60-km segments along the bore axis. A 30-km-wide cloud field accompanied the mature bore system within three hours of its formation. System-relative airflow within the cloud field was front-to-rear and exhibited a primary hydraulic jump updraft (4–5 m s^{-1} magnitude) within the bore core. The bore core exhibited a low, smooth cloud base, a cloud depth of 2.5 km, nearly adiabatic liquid water content, and pronounced turbulence. The maximum parcel displacements within the bore were about 2 km (sufficient for marginal convective initiation), and the net parcel displacement from before to after bore passage was 0.6–0.9 km.

1. Introduction

This paper examines the formation and evolution of an atmospheric internal bore that was initiated by a strong gust front within a developing (unsteady) nocturnal boundary layer (NBL). The complete evolutionary cycle, from a gust front to a bore to an eventual solitary wave pair, is examined with radar, profiler, and surface observations. The evolution of the NBL thermodynamic and wind profiles is also resolved with radar and atmospheric profiling measurements to relate convergent boundary zone (CBZ[1]) evolution to NBL changes.

Gust fronts define the leading discontinuity of an initial diverging thunderstorm outflow or, in the mature stage, a propagating gravity current. A typical gravity current consists of an elevated head near the leading edge, a rear-to-front feeder flow within the lower portion of the current, and an updraft ranging between 1 and 10 m s^{-1} (3–5 m s^{-1} is typical) around the leading edge (Goff 1976; Wakimoto 1982; Droegemeier and Wilhelmson 1987; Simpson 1997). Changes in the surface wind vector and thermodynamics during the gust front passage are typically large and coincident.

When static stability is sufficiently high near the surface, bores and solitary waves are produced when gust fronts force the stable air upward. Like gust fronts, many atmospheric bores are typified by a significant surface wind shift in the direction of propagation, a pressure rise, and energetic updrafts (Clarke et al. 1981). Changes in surface temperature (T) can be variable, ranging from negligible (Mahapatra et al. 1991) to modest T increases, produced by mixing of warm air

[1] A CBZ refers to any convergent flow within the atmospheric boundary layer. In this paper, CBZ is used generally to identify a gust front, bore, or gravity wave.

Corresponding author address: Dr. Kevin R. Knupp, Dept. of Atmospheric Science, University of Alabama in Huntsville, NSSTC, 320 Sparkman Drive, Huntsville, AL 35805.
E-mail: kevin.knupp@nsstc.uah.edu

down to the cool surface (Clarke et al. 1981), to modest cooling and/or drying associated within arrival of the residual gravity current air following the surface wind shift (Fulton et al. 1990; Koch et al. 1991; Koch and Clark 1999).

A solitary wave exhibits minor surface wind vector changes in the form of a weak convergent/divergent couplet and a surface pressure oscillation associated with adiabatic ascent/descent of stable air (Doviak and Ge 1984). The primary difference between a solitary wave and a bore is that upward parcel displacements are long-lasting in the wake of the bore hydraulic jump, whereas the net parcel displacement for a solitary wave is negligible across the width of the disturbance (Christie et al. 1978). Consequently, surface pressure remains high after bore passage (e.g., Koch and Clark 1999), but oscillates to a maximum and then to near the preexisting value during a solitary wave passage (Christie 1989; Doviak et al. 1991).

Field observations of atmospheric bores have been reported since the work of Tepper (1950). Knowledge of bores increased as the morning glory, a common bore phenomenon along the coast of northeastern Australia, solicited the interest of researchers (Clarke et al. 1981; Christie et al. 1978; Christie 1989; Smith 1988). Subsequent idealized numerical simulations of bore phenomena have disclosed additional details on their dynamics (Crook and Miller 1985; Crook 1986; Christie 1989; Smith and Noonan 1998; Goler and Reeder 2004). Other observational studies of bores and solitary waves utilizing Doppler radar, Doppler sodar, surface data, and other remote sensors have been conducted by Doviak and Ge (1984), Cheung and Little (1990), Fulton et al. (1990), Mahapatra et al. (1991), Wakimoto and Kingsmill (1995), Kingsmill and Crook (2003), and Demoz et al. (2005). In addition to these, a few investigations have used Doppler wind profilers to determine bore properties (Ralph et al. 1993, 2000; Koch and Clark 1999).

In this paper, we present an analysis of a gust front to bore to solitary wave transition that occurred during the early to middle stages of the NBL cycle. The synoptic environment is summarized in section 3. An overview of the CBZ evolution is presented in section 4. The evolution of this CBZ is summarized in Fig. 1 as simplifications to the observed or inferred structures at the times indicated. Low-level stabilization within the NBL, expressed as an increase in Brunt–Väisälä frequency (N_{BV}), increased throughout the period (section 5). As the parent gravity current dissipated, the mature bore emerged as a separate entity, and a secondary wave developed along an elevated inversion in advance of the bore (Fig. 1b). The analysis of these structures is presented in section 6. This disturbance then evolved to a dual-crested solitary wave (Fig. 1c), and ultimately to a single (solitary) wave that propagated along an elevated inversion. Section 7 presents a discussion of the results, and conclusions follow in section 8.

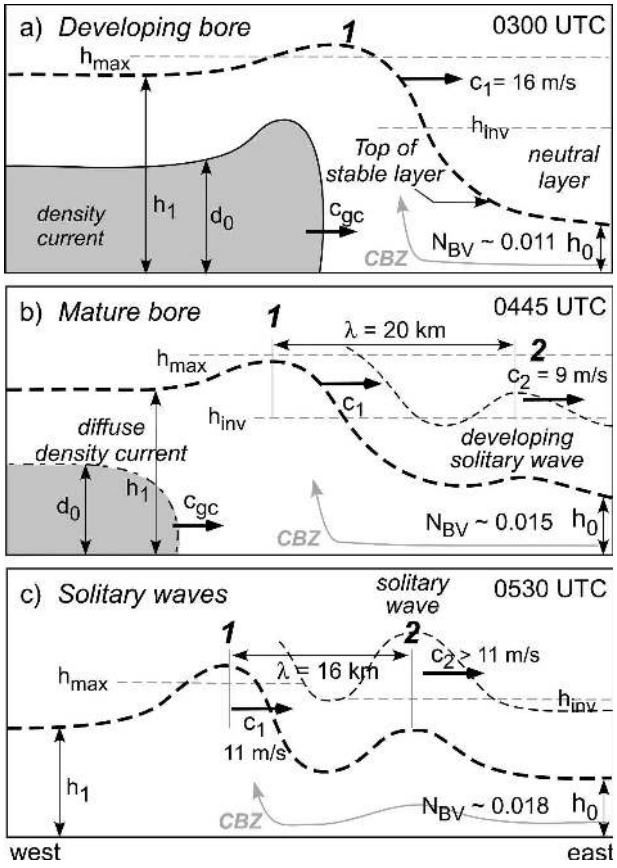

FIG. 1. Schematic vertical cross section showing the transition from a gust front/bore to an eventual solitary wave pair. The three stages include the (a) developing bore, (b) mature bore, and (c) solitary waves 1 and 2. The NBL depth (h_0) and stability [expressed in terms of Brunt–Väisälä frequency (N_{BV}, units of s^{-1})] both increased during this sequence. The heavy dashed line represents the top of the stable layer, and h_1 represents the mean bore depth. The thin dashed line (θ = const) is drawn to delineate the leading solitary wave, labeled 2. The shaded region in (a) and (b) denotes cool, dry air associated with the gravity current of depth d_0. The solid gray streamline represents low-level relative flow that defines the CBZ associated with the bore. The initial bore formed in advance of the gust front by 0300 UTC. A second solitary wave formed within the elevated inversion layer (h_{inv}) in advance of the bore about 30 min before the time in (b). By 0500 UTC, the gravity current disappeared. Propagation speeds of the gravity current and two buoyancy waves are represented by c_{gc}, c_1, and c_2.

2. Data

The primary data are derived from the University of Alabama in Huntsville Mobile Integrated Profiling System (MIPS), the National Center for Atmospheric Research (NCAR) S-band dual-polarization Doppler radar (S-Pol), and profiling instrumentation, all located in the Oklahoma panhandle at or near a site termed "Homestead" (16 km east of the S-Pol radar). The MIPS was operated in a mobile mode during the International H_2O Project (IHOP) conducted during May–June 2002 (Weckwerth et al. 2004). For this particular case, the MIPS was deployed at a location close to the S-Pol radar and Homestead for a boundary layer evolution experiment on 21 June 2002. Figure 2 shows the relative locations of instruments.

The MIPS instruments included a 915-MHz Doppler wind profiler[2] (915), a 12-channel microwave profiling radiometer (MPR), a lidar ceilometer, a Doppler sodar, and surface instrumentation. Operating parameters and measurements characteristics for each instrument, and a picture of the MIPS configuration for IHOP, are presented in Karan and Knupp (2006). Additional characteristics of the MPR can be found in Solheim et al. (1998), Güldner and Spänkuch (2001), and R. Ware et al. (2004, unpublished manuscript, available from http://www.radiometrics.com/pubs.html).

The NCAR S-Pol radar was utilized during IHOP to measure reflectivity factor (Z), radial velocity (V_r), differential reflectivity (Z_{DR}) and other dual polarization variables, and refractive index (N) derived from phase measurements of ground clutter targets (Fabry 2004). S-Pol scans were acquired at low elevation angles (0.0°, 0.5°, 1.2°, 2.0°, 3.0°, and 4.0°) at 5-min intervals. Range gate spacing was 150 m, and the azimuth spacing between successive beams was about 0.85°.

Several instruments at Homestead were utilized in this study to provide additional details on, or clarification of, NBL and CBZ properties: (i) the NCAR 915-MHz Multiple Antenna Profiler Radar (MAPR), (ii) the University of Wisconsin Atmospheric Emitted Radiance Interferometer (AERI), and (iii) the National Aeronautics and Space Administration (NASA) Goddard lidar Observatory for Winds (GLOW).

Surface data were analyzed from the MIPS (1-s resolution), NCAR portable automated mesonet stations (1-min resolution), NCAR surface flux stations (5-min resolution), and the Oklahoma Mesonet (5-min resolution).

[2] The radial velocity along the zenith beam is defined as W, which is not necessarily vertical motion w because of possible contributions from insect motion.

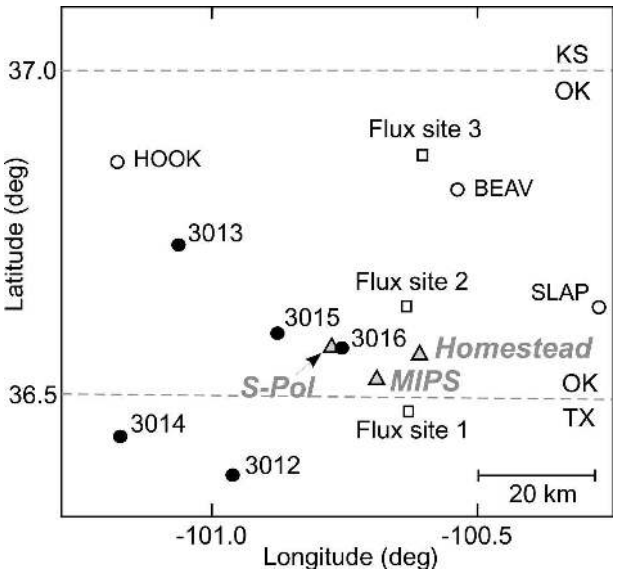

FIG. 2. Locations of instrumentation used during the IHOP project. Open circles are Oklahoma Mesonet sites, solid circles are NCAR mesonet sites, open boxes are NCAR surface flux sites, and triangles are radar or profiling sites.

3. Synoptic overview

Synoptic patterns at 0000 UTC 21 June are presented in Fig. 3. The IHOP domain was beneath an elongated 500-hPa ridge and associated weak flow that extended from the Texas panhandle to the Ohio Valley. Stronger southerly flow at low levels (Fig. 3b) was produced by an enhanced pressure gradient located between high pressure centered over the eastern United States and a broad low pressure region from western Colorado to Nevada. The relatively strong pressure gradient produced a low-level 20 m s^{-1} southerly jet (within the 300–500-m AGL layer) in advance of the CBZ by 0200 UTC.

A significant inversion capped the atmospheric boundary layer (ABL) over the region (Figs. 4a,b), producing convective inhibition (CIN) ranging from −180 to −220 J kg^{-1} between Amarillo, Texas (AMA), and Dodge City, Kansas (DDC). An east–west gradient in CIN was analyzed at 0000 UTC (Fig. 3a) from Homestead, where CIN was between −100 and −200, to the New Mexico border, where CIN was negligible.

Organized deep convection formed within a narrow zone of high CAPE (>2500 J kg^{-1}) and low CIN over eastern New Mexico and southeastern Colorado during the afternoon hours. This deep convection coalesced and moved eastward, forming a 500-km long (north–south) quasi-linear mesoscale convective system (MCS) that was located near the eastern New Mexico border

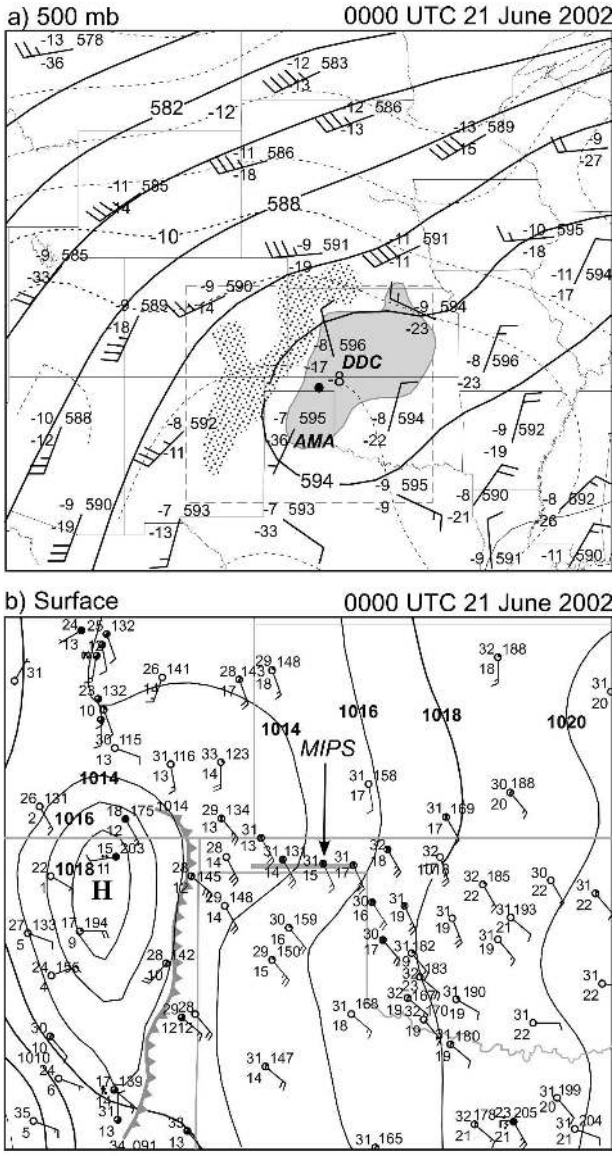

FIG. 3. (a) Regional 500-hPa analysis for 0000 UTC 21 Jun 2002. Station plots include temperature and dewpoint temperature (°C), geopotential height (decameters), and wind barbs (one full barb represents about 5 m s^{-1} or 10 kt). Contours are geopotential height (solid lines, labeled in decameters) and temperature (dashed lines, labeled in °C). The coarse stippled region represents CAPE > 2500 J kg^{-1}, and the gray shaded region denotes CIN < -100 J kg^{-1}. The MIPS is located at the black-filled circle in the Oklahoma panhandle. (b) Surface analysis at 0000 UTC 21 Jun 2002. Isobars are drawn every 2 hPa. Temperature and dewpoint temperature are plotted in °C, and pressure is denoted in standard coded form. A full wind barb represents 5 m s^{-1} (10 kt). A mesohigh and gust front produced by a line of active deep convection over eastern New Mexico is shown.

by 0100 UTC. This MCS generated an extensive region of cool surface air and high pressure. A long gust front extending from southeastern Colorado to southeastern New Mexico at 0000 UTC (Fig. 3b) interacted with the developing NBL and produced the bore and solitary waves that are the subjects of this study.

4. CBZ evolution

a. CBZ propagation

The evolution of the radar fine line is depicted in Fig. 5 for the 0251–0555 UTC period. CBZ propagation speeds (bold numbers, m s^{-1}) decreased significantly around the middle part of this period, from 15.9 m s^{-1} at 0251 to 10.8 m s^{-1} at 0555 UTC. For the initial 1-h period of this sequence, the CBZ exhibited a wavy structure with distinct Z maxima, particularly over its southern portion. The shape transformed to a smoother linear structure with less variability in Z after 0412 UTC, suggesting a transformation in CBZ properties. Following a gradual reduction in Z after 0513, the fine line disappeared after 0600 UTC due to a combination of CBZ weakening and poorer radar sampling at long range.

b. Changes in surface properties

Data from four surface stations along an east–west line about 200 km long are presented in Fig. 6. Locations of three of these stations are shown in Fig. 5. Important features shown in the time series of T, dewpoint temperature (T_d), pressure (p), and wind are summarized in the following:

(i) A pressure rise of 1–2 hPa was measured during a 1-h period preceding the CBZ arrival for all four stations. This pressure increase terminated as a relative maximum value (labeled 2 in Figs. 6c,d) 30–40 min before the wind shift associated with the bore.

(ii) The decrease in prebore surface temperature, from 27°C at BOIS at 0130 UTC (4°C less than the afternoon maximum) to 24°C at SLAP (at 0400 UTC), implies an increase in NBL stability (described in section 5a) between these two locations and times.

(iii) The temperature reduction across the bore decreased over the 80 km distance from BOIS (−8°C) to GOOD (−3.5°C).

(iv) The maximum wind speed (westerly) following bore passage decreased from BOIS (14 m s^{-1}) to Station 3016 (7 m s^{-1}). At both locations, this maximum value was less than the bore propagation speed.

(v) Although the time series at BOIS and GOOD are similar to changes produced by a gust front, the pressure increase in advance of the wind shift suggests the presence of a developing (strong) bore.

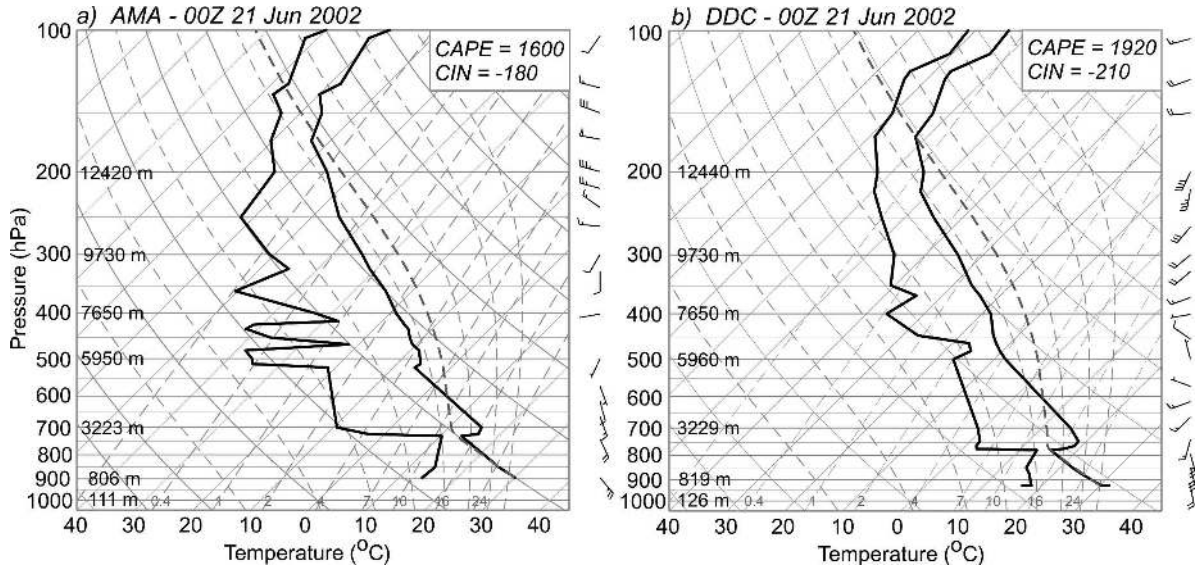

FIG. 4. NWS soundings, plotted on a skew T–ln p diagram, for DDC and AMA at 0000 UTC 21 Jun 2002. Locations are annotated in Fig. 3a. The curved dashed line represents a parcel path based on averages of potential temperature and mixing ratio over the lowest 500 m.

(vi) The time series at SLAP typifies the passage of a two crested solitary wave (i.e., two maxima in p) near 0500 UTC. Wind changes are present but subtle, and thermodynamic variations are absent.

5. NBL evolution

In this section the time-dependent nocturnal boundary layer properties at the MIPS and Homestead loca-

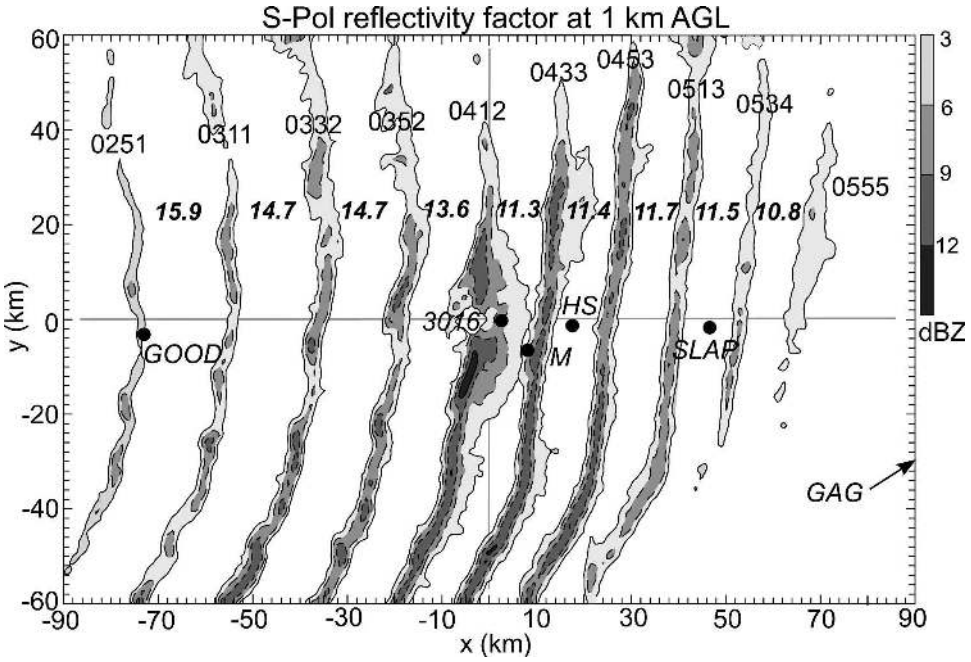

FIG. 5. The radar fine line associated with the bore/solitary wave is shown as contours of reflectivity factor (derived from the S-Pol radar located at the origin) interpolated to the 1 km AGL level. The translational speed is represented by bold numbers, and the time of each segment is identified in UTC at the top of the figure.

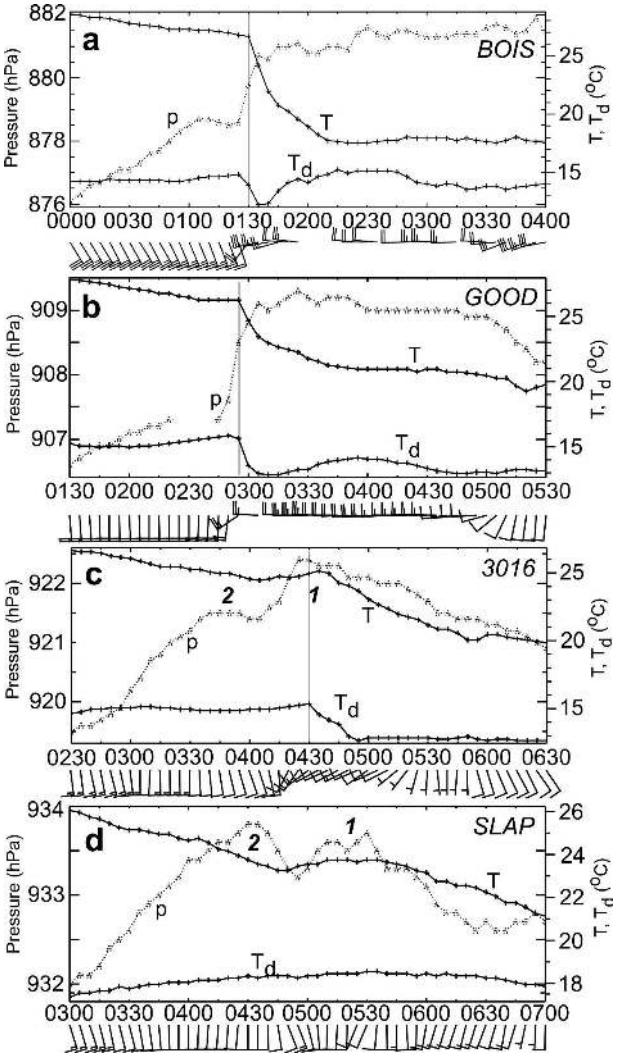

FIG. 6. (a)–(d) Time series of surface data from four meteorological stations. The locations of GOOD, 3016, and SLAP are plotted in Fig. 5. Thin vertical gray lines in (a)–(c) denote time of initial decrease in dewpoint temperature. Relative pressure maxima, labeled 1 and 2, correspond to disturbances 1 (bore that transformed to a solitary wave) and 2 (solitary wave). Wind barbs at the bottom of each panel follow standard convention, with one full barb representing 5 m s^{-1} (10 kt). Time along the horizontal axis is labeled in UTC.

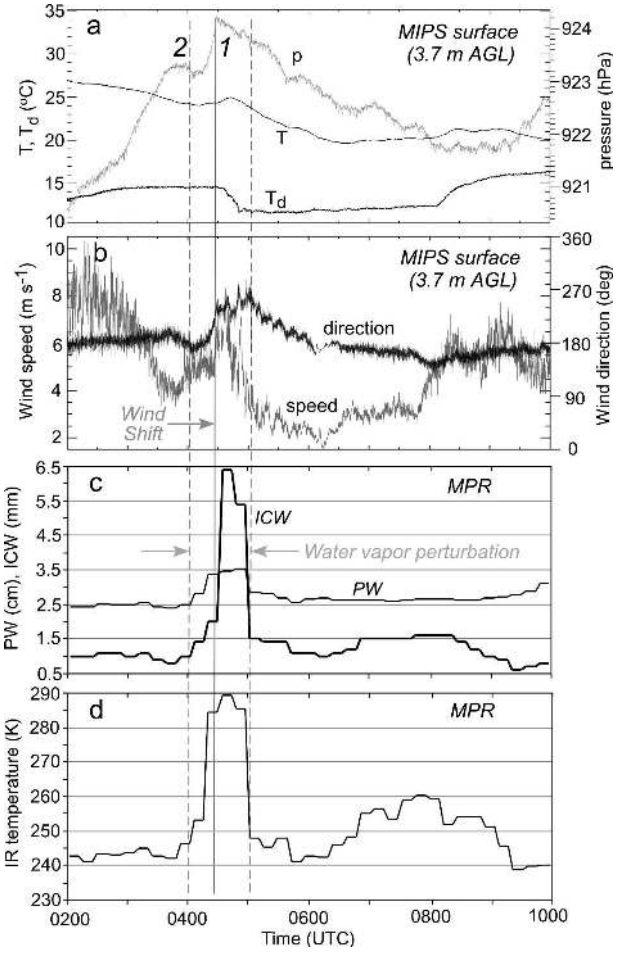

FIG. 7. MIPS surface measurements of (a) temperature, dewpoint temperature, and pressure and (b) wind speed and direction. Data are plotted at 1 Hz. Values derived from the microwave profiling radiometer at 14-min intervals include (c) precipitable (PW) and integrated cloud water (CW), and (d) IR temperature at vertical incidence.

tions are examined during the 0200–0600 UTC time period.

a. Thermodynamics and stabilization of the NBL

In this case, the NBL development was accelerated by shading from the MCS anvil. This cooling had occurred by 0130 UTC over the lowest 200–300 m (prior to sunset at 0204 UTC) and eventually reached 800 m AGL owing to negative vertical heat flux from sustained shear-generated turbulence. Time series of MIPS surface parameters during the 0200–0400 UTC period (Figs. 7a,b) show a steady decrease in T (27° to 24°C), mean wind speed (8 to 4 m s^{-1}), and wind gusts, all of which indicate stabilization. The sodar backscatter power (not shown) revealed an increase in enhanced signal below 200 m between 0130 and 0415 UTC, indicative of a strengthening vertical temperature gradient. The deepening of the stable NBL is also corroborated in the MPR potential temperature (Fig. 8a).

Four Radio Acoustic Sounding System (RASS) soundings (Fig. 9) illustrate variations in virtual temperature (T_v) before and after the bore passage. A weak inversion developed below 130 m, and a near-isothermal layer extended up to 500 m between 0303 and 0403 UTC. A net reduction in T_v followed the bore passage (between 0403 and 0503 UTC), and the inver-

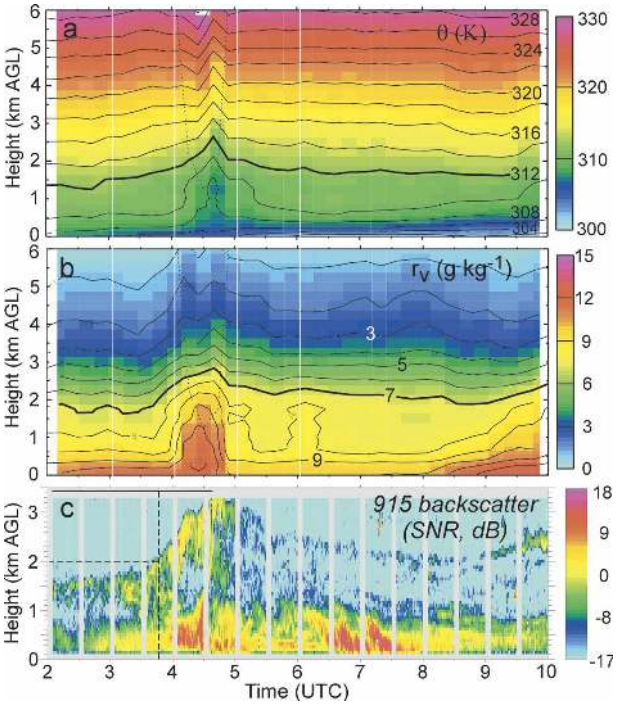

FIG. 8. Time vs height section of (a) potential temperature (K) and (b) water vapor mixing ratio (g kg^{-1}) derived from the microwave profiling radiometer. (c) Backscatter power; (SNR; in dB) from the 915-MHz profiler. The passage of the CBZ was associated with cool, moist air and an increasing depth and intensity of 915-MHz backscatter. Vertical white lines in (a), (b) denote RASS soundings shown in Fig. 9.

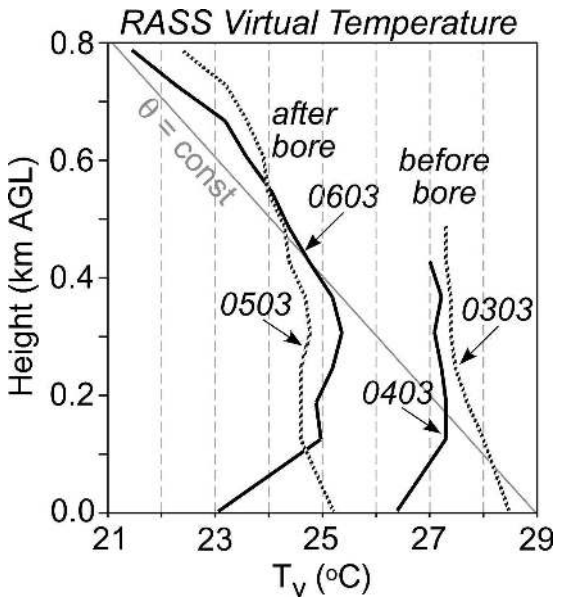

FIG. 9. Profiles of virtual temperature derived from the MIPS RASS in advance of the bore (0303 and 0403 UTC), and in the wake of the bore (0503 and 0603 UTC).

sion was reestablished by 0603 UTC after clouds associated with the bore receded. A composite sounding at 0345 UTC, shown in Fig. 10, is based on the MIPS RASS, MPR, and 915-MHz signal-to-noise ratio (SNR), the Homestead AERI, and 0000 UTC National Weather Service (NWS) soundings at AMA and DDC. The SNR was used to determine the (rising) inversion level near 2 km at 0345 UTC, which was not well resolved by either the MPR or AERI due to inadequate vertical resolution at this level. The residual mixed layer below 2 km and the elevated nearly neutral layer above 2 km (Fig. 4) are represented in the composite sounding. The uncertainty in the elevated inversion structure and overlying neutral layer is depicted by an additional dashed gray line between 73 and 60 kPa. The surface-based NBL inversion and the inversion near 2 km represent the most significant stable layers in this sounding. At 0345 UTC, the average Brunt–Väisälä frequency ($N_{BV} = [(g/\theta)(\Delta\theta/\Delta z)]^{1/2}$) over the lowest 700 m is 0.015 s^{-1}.

b. Wind profile evolution

The wind profile evolution in Fig. 11 reveals appreciable changes around the time of bore passage. Southerly flow over the lowest 1 km veered about 30° between 0300 and 0430 UTC. The wind profile exhibited less veering with respect to height below 1.5 km, although above 1.5 km a substantial veering was measured by the MAPR within the 1-h period before the bore passage. The wind perturbation associated with the bore, highlighted by the gray line in Fig. 11, reveals the bore passage between 0430 and 0630 UTC. Southerly flow and increasing low-level water vapor were reestablished after 0700 UTC (Fig. 8b).

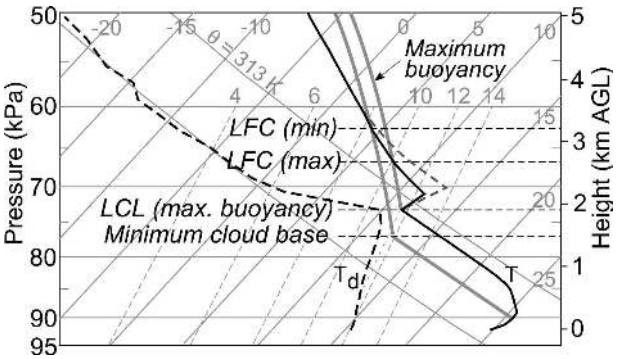

FIG. 10. Composite sounding of temperature and dewpoint temperature at 0345 UTC, plotted on a skew T–ln p diagram. This sounding represents the environment 45 min before the CBZ passage. Two profiles of T (black and gray dashed) between 73 and 60 kPa represent the uncertainty in this layer. Two parcel paths are shown: the most unstable parcel (producing a minimum in CIN) that originates in the residual layer above the NBL, and a parcel (originating from the NBL) that corresponds to the lowest measured cloud base (1.4 km) during bore passage.

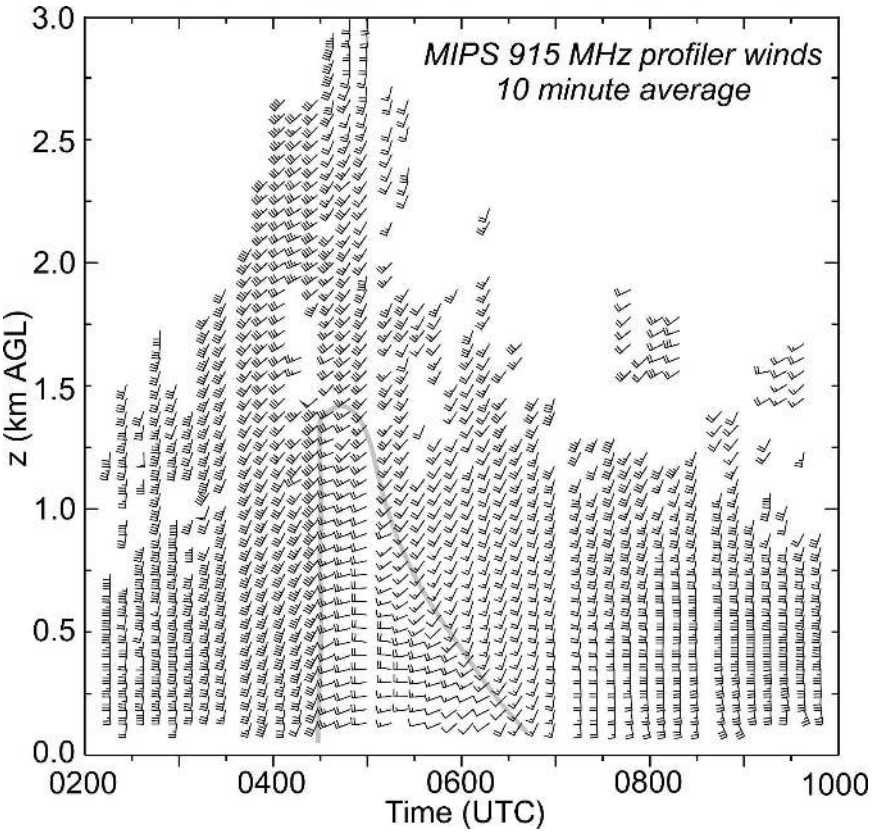

FIG. 11. Time–height section of horizontal wind derived from the MIPS 915-MHz wind profiler. Each profile is spaced by 10 min and is based on a 10-min average of the radial wind components. The gray solid line demarks the period of significant westerly flow associated with the CBZ.

Profiles of the u and v wind components and potential temperature at 0345 UTC (50 min before the bore arrival at the MIPS site) are displayed in Fig. 12. The u component (normal to the CBZ) has uniform linear positive shear, with u increasing from about 1 m s^{-1} at the surface to 10 m s^{-1} at 2 km. The v profile (approximately parallel to the CBZ) exhibits an 18 m s^{-1} jet near 0.5 km AGL and significant shear below 200 m. The temporal veering of the wind prior to bore passage suggests confluence related to convergence and mesoscale ascent [section 6b(2)].

6. Analysis of the CBZ

Analyses of radar and profiler data during the 0330–0530 UTC period presented in the following subsections describe the formative to mature stages of the bore and its transformation to a solitary wave pair.

a. Bore development (0130–0330 UTC)

Time series of surface data (section 4b) suggest initial bore formation by 0130 UTC. The airflow within a vertical east–west plane perpendicular to the bore at 0332 UTC is presented in Fig. 13a. This analysis assumes that the bore airflow is two dimensional with uniform flow along the y (south–north) direction. Because the maxi-

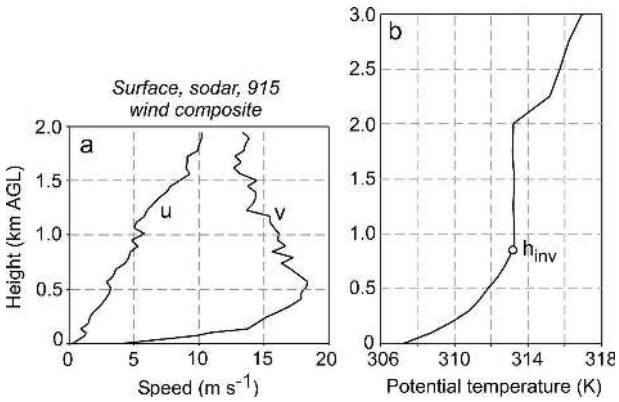

FIG. 12. Vertical profiles of (a) the u (zonal) and v (meridional) wind components at 0345 UTC, derived from the MIPS 915-MHz profiler, Doppler sodar, and surface instruments and (b) potential temperature based on the composite sounding in Fig. 10.

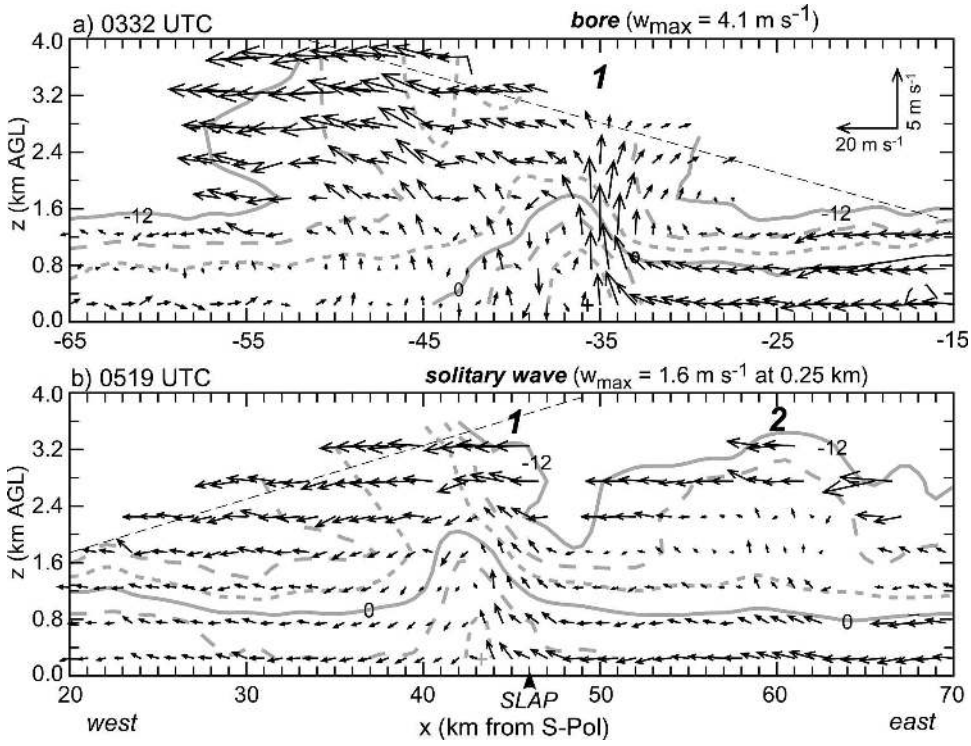

FIG. 13. Airflow (relative to the moving CBZ) and Z analyses within a vertical west–east plane derived from S-Pol Z and V_r data at 0332 and 0519 UTC. The S-Pol radar is at the origin. (a) The CBZ (labeled 1) assumes the form of a bore near $x = -35$ km. (b) CBZ assumes the form of an initial solitary wave (labeled 1) near $x = 45$ km, and a secondary solitary wave (labeled 2) near $x = 60$ km. This plane is approximately normal to the CBZ at both times. Reflectivity factor Z is contoured every 4 dB beginning at -12 dBZ. The SLAP surface station location (very close to the plane of this figure), whose data are plotted in Fig. 6d, is marked in (b).

mum S-Pol elevation was 4.0°, a range of 35–40 km was required to sample the CBZ throughout most of its depth. S-Pol Z and V_r data were interpolated to a Cartesian grid with 0.5 km spacing in all three directions. The lowest horizontal plane in this grid was set at 250 m AGL in order to resolve the gravity current feeder flow. The Z and V_r fields were smoothed with a Hanning filter and then averaged over a 5-km interval in the y direction, centered on the x axis ($x = 0$). The vertical wind component was derived from integration of the anelastic mass continuity equation, $\partial(\rho w)/\partial z = -\partial(\rho u)/\partial x$, using a variational constraint, and applying top and bottom boundary conditions that were a fraction (1.0 and 0.5) of the vertical grid increment (500 m) multiplied by the value of divergence at the lowest (0.25 km AGL) and highest sampling levels.

The primary updraft is located along the forward gradient of the fine line Z contours centered at $x = -37$ km. The maximum analyzed updraft is 4.1 m s^{-1} near 1.0 km AGL (typical of gust front updrafts), but this value is likely underestimated because of resolution limitations (at 35-km range) and incomplete sampling throughout the entire depth, limited by the 4.0° maximum elevation angle. A gravity current feeder flow is absent in this system-relative frame, except west of $x = -50$ km (about 15 km behind the CBZ).[3] The absence of the feeder flow, in addition to the moderately strong stability ($N_{BV} = 0.015$ s^{-1}) over the lowest 700 m, supports the premise that the CBZ had assumed bore characteristics at this time. Low-level easterly flow approached the CBZ primarily below 1 km AGL (the stable layer). A 25-km-wide cloud field (defined by the -12-dBZ contour) extended up to 4 km AGL within and west of the CBZ. The upper trailing portion of this cloud exhibits a pronounced front-to-rear flow, weak updraft (<1 m s^{-1}), and moderate vertical shear (4.5×10^{-3} s^{-1}) between 1.5 and 3.5 km AGL.

Oscillations in W are apparent west of the CBZ as three narrow updrafts near 1 km AGL spaced about 4–5 km apart. For a speed of 14.7 m s^{-1}, this spacing

[3] Although radar resolution is limited at a range of 40 km, surface data, and S-Pol V_r patterns at later times (closer range) support the absence of the feeder flow.

translates to a wave period of about 300 s, which compares to the mean Brunt–Väisälä period of 400 s (based on the θ profile in Fig. 12b).

Although the CBZ exhibited gravity current characteristics during this period, the following observations are consistent with the formative stages of a bore: (i) The ambient NBL stability was sufficient to sustain a bore. (ii) The trailing cloud field was broad (25 km), unlike the narrow cloud fields that typically accompany gust fronts and weak bores. (iii) A feeder flow was absent to the rear of the CBZ. (iv) The observed 15 m s^{-1} propagation speed exceeds the theoretical gravity current speed [section 7a(2)] by almost 50%.

b. *Mesoscale structure of the bore at maturity (0430–0530 UTC)*

1) S-POL MEASUREMENTS

Figure 14 presents Z and V_r patterns associated with the mature bore and adjacent wave structures at 0434, 0456, and 0516 UTC. The solid line (Fig. 14b) defines the approximate leading edge of the bore cloud field, based on the S-Pol −12-dBZ contour. The rear (west) part of the system is represented with less definition by a 17 m s^{-1} westerly inflow jet within the 400–500-m-AGL layer. Most pronounced 30–50 km west of the bore, this jet was a remnant of the gravity current feeder flow and weakened with time and increasing distance east of S-Pol.

Figure 14b shows modest convergence (much weaker than at 0332 UTC) defined by the white dashed line. The Z fine line, labeled "1" in Fig. 14a, is diffuse below 0.5 km AGL. Its definition sharpens above this level at later times (Figs. 14c,d). At heights below 1 km, the fine line was better defined south of S-Pol than to the north. Likewise, the lateral shear along the bore leading edge was more concentrated to the south (Fig. 14b). At 0415 UTC, a narrow band of enhanced 18–20 m s^{-1} southerly flow in the 0.3–0.5-km-AGL layer preceded the CBZ as it passed directly south of S-Pol. A similar jetlet was analyzed in advance of a bore by Koch and Clark (1999). As the bore moved over and east of the S-Pol radar, both convergence inferred from V_r, and the fine line definition in Z became less distinct. The MIPS 915-MHz profiler and NCAR MAPR (section 6c) measured weak updraft below 1 km AGL during passage over those sites around this time, confirming that low-level convergence had decreased.

A weak gradient in low-level T_d was analyzed in refractivity (N) estimated from S-Pol phase change measurements (Weckwerth et al. 2005). Isodrosotherms derived from this analysis (which assumes a constant temperature of 25°C) are the black dashed lines (labeled in °C) in Fig. 14b. This pattern displays a rather diffuse low-level water vapor gradient rearward of the CBZ, consistent with surface observations and time series around this time.

A second linear band of enhanced Z (labeled 2 in Figs. 14c,d), most apparent between 1.4 and 3.0 km AGL, was located in advance of the bore at 0434, 0456, and 0516 UTC. This band is more prominent in the Z field at 2.0° (near cloud base about 2 km AGL, not shown) where scattering from cloud droplets is suggested. S-Pol measurements imply that wave 2 was not rooted to the NBL, as Z_{DR} values were near zero, which implies cloud droplets. In contrast, Z_{DR} values associated with the bore (wave 1) exceeded 4 dB below 1.5 km, indicating the presence of insects and therefore a direct connection to the NBL.[4] Because wave 2 corresponds to the relative pressure maximum labeled as 2 in Figs. 6c,d and 7, it exhibits properties of a buoyancy (solitary) wave that was not rooted within the lowest 1 km where insects were common. The MIPS ceilometer measurements (next section) did not detect the cloud associated with this wave, so cloud formation occurred after 0410 UTC. The S-Pol radar measurements suggest a first echo by 0412 about 10 km east of the MIPS. The propagation speed of this wave (9.2 m s^{-1}) was about 80% of the 11.3 m s^{-1} bore propagation speed.

Shorter wavelength multiple bands in Z (labeled 1A and 1B in Fig. 14) were detected between 0416 and 0530 UTC. They portray a structure similar to that of an undular bore, but their formation differs from previous observations of bore evolution. For example, wave 1B appeared at 0416 UTC about 4 km in front (east) of the main CBZ. By 0456 UTC, wave 1B was most apparent as a 30-km-long segment centered 30 km northeast of S-Pol (Figs. 14a,c). Since its propagation speed was 14.2 m s^{-1}, about 25% greater than that of the main CBZ, the separation distance increased with time. This wave also appears to have roots within the NBL, as Z_{DR} values exceed 5 dB (insect scattering). Another significant wave (labeled 1A in Fig. 14a) developed by 0434 UTC 12 km behind the CBZ north of S-Pol. This wave was also filled with high Z_{DR} values. An extension of this wave appears about 50 km south of S-Pol at 0456 UTC. This wave may be classified as a lee wave that formed in the wake (relative downwind direction) of the CBZ. Formation of secondary waves behind the leading (high amplitude) wave is a more typical mode of secondary wave generation (e.g., Christie 1989). This

[4] The insect layer, defined by $Z_{DR} > 4$ dB and $Z > -7$ dBZ, extended to about 0.9 km AGL, or just above the NBL height. Insects are known to produce high Z_{DR} values (Zrnić and Ryzhkov 1998).

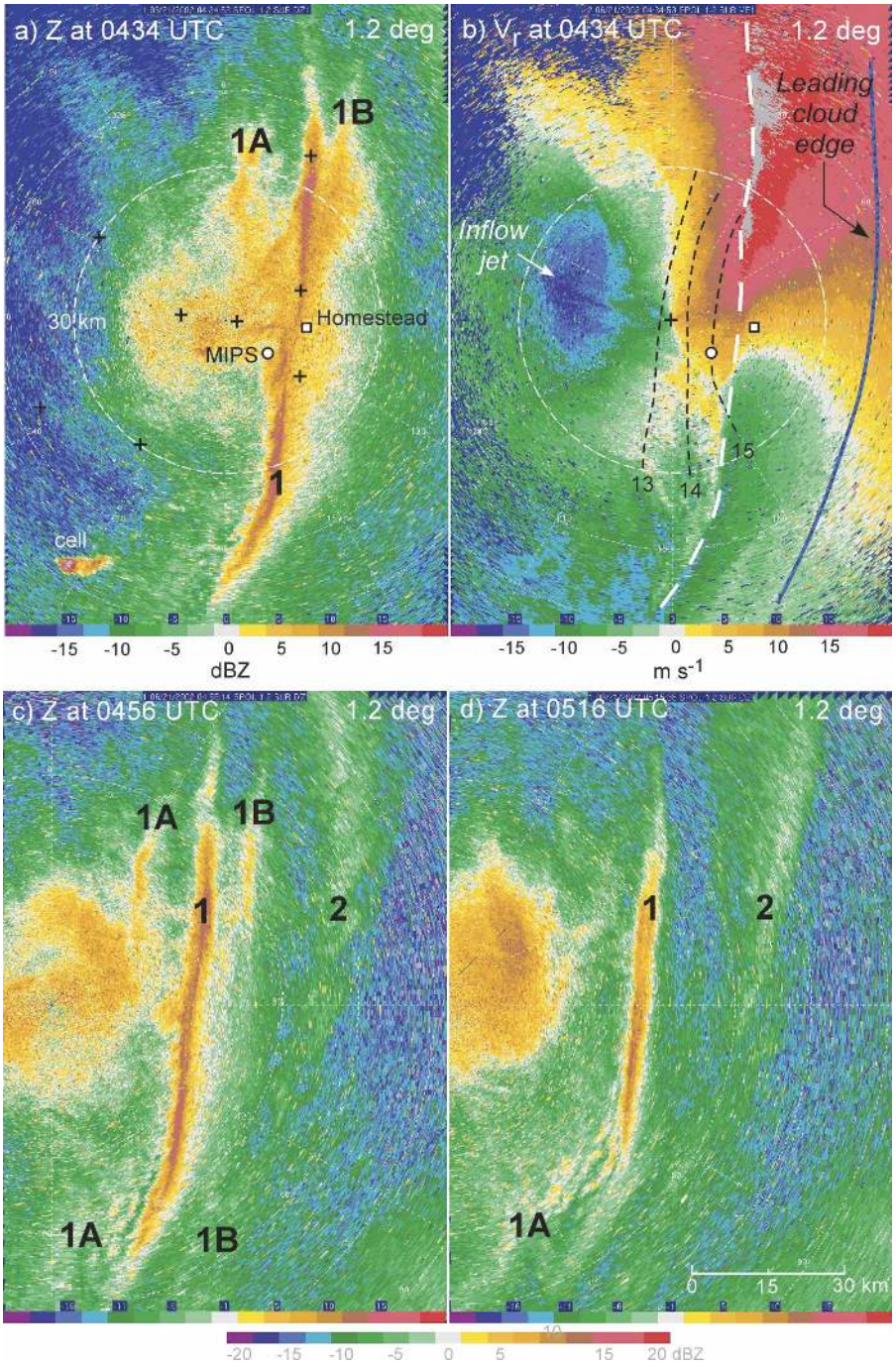

FIG. 14. S-Pol plan position indicator scan (1.2° elevation angle) of (a) reflectivity factor (Z) and (b) radial velocity (V_r) at 0434 UTC. The scale for each field is shown at the bottom of (d). In (b) the dashed black lines are dewpoint temperature, labeled in °C, derived from the S-Pol refractivity measurement (at 0° elevation angle) assuming a temperature value of 25°C. The dashed white line denotes the CBZ location, and the solid blue line marks the leading edge of the cloud field at 0434 UTC. (c), (d) As in (a) except for 0456 and 0516 UTC.

wave was most apparent as a segment about 60 km long, centered about 60 km south of S-Pol. Its orientation (215°–35°) would have exposed it to the jet profile of the v wind component; hence this wave segment experienced much different shear (and hence ducting) conditions. It disappeared after 0540 UTC after having been a prominent feature for about 1 h. This transient behavior suggests an evolving and inhomogeneous

NBL and demonstrates the complexities that develop when a CBZ experiences locally different low-level wind shear and stability (e.g., Christie 1989).

2) MIPS MEASUREMENTS

(i) Formation of the leading solitary wave

The initial pressure maximum near 0345 UTC at the MIPS location (labeled 2 in Fig. 7a) corresponds to the subsequent leading cloud band annotated in Figs. 14c,d. The absence of ceilometer backscatter around 0345 UTC (Fig. 15c) indicates that this cloud had not yet formed over the MIPS site (Fig. 15c). However, an increase in the MPR precipitable water (PW) immediately followed the pressure maximum. Although the passage of this wave did not affect surface thermodynamics, a slight oscillation in wind speed and direction (consistent with weak convergence) was measured. Such convergence implies weak updraft and the production of cold air by adiabatic ascent within stable air. Surface data (Fig. 6d) show that the magnitude of wave 2 increased as it propagated eastward; indeed, the S-Pol measurements presented in the previous section corroborate this inference.

(ii) Mesoscale kinematics

At horizontal scales >5 km, the bore kinematics as portrayed in the time versus height section of horizontal wind (Fig. 11) appear simple. During passage over the MIPS, a shift from southerly to westerly flow occurred over a 1.5-km-deep layer within the head after which the depth of this flow perturbation decreased with time. This flow exhibits the head structure of the parent gust front, which has also been simulated for gust front to bore transition by Liu and Moncrieff (2000).

Figures 15 and 16 reveal a laminar flow with weak ascent between 0330 and 0430 UTC above 1.5 km AGL. A time series of W from the MAPR at 1.0, 1.7, and 2.5 km AGL (Fig. 17) reveals mean ascent of about 0.5 m s^{-1} during this period. A similar updraft magnitude is also inferred by the monotonic increase in height of the MIPS 915-MHz relative maximum in SNR (Fig. 15a) from 2.0 to 3.0 km AGL over the 0340–0414 UTC period (a mean updraft of 0.49 m s^{-1}), and by the rise in the MAPR 0-dB SNR contour (Fig. 16a) from 2.1 to 3.2 km AGL layer over the 0348–0422 UTC period (a mean updraft of 0.54 m s^{-1}). These calculations assume that ascent of a constant SNR surface is due to vertical motion, and not horizontal advection.

The bore passage at the MIPS site was accompanied by an increase in aerosol backscatter below 500 m AGL

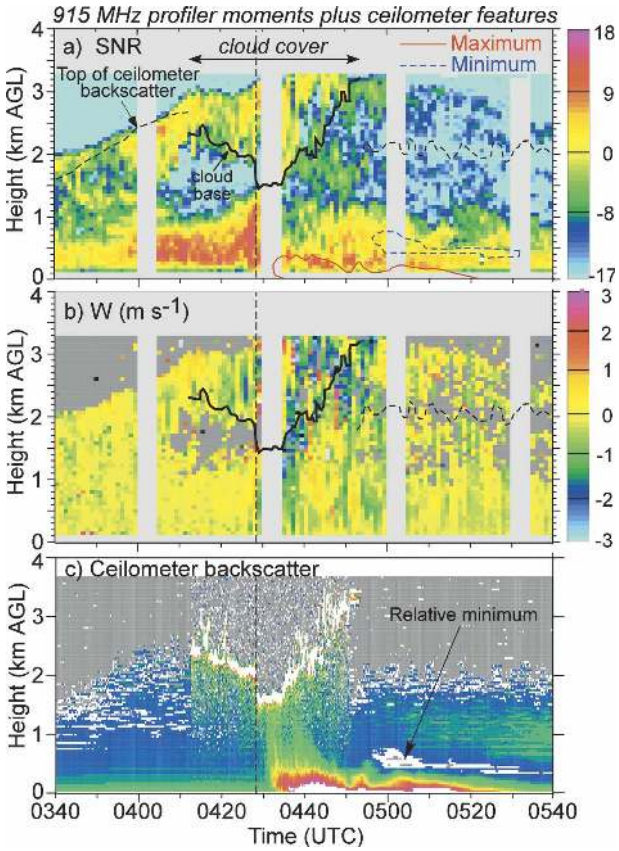

FIG. 15. MIPS 915-MHz profiler time vs height sections of (a) SNR and (b) Doppler velocity (W), both derived from the vertical beam. The temporal resolution is 60 s. (c) The ceilometer backscatter indicates cloud base and relative variations in aerosol backscatter at 15-s temporal resolution. Ceilometer features such as cloud base, top of backscatter, and locations of high and low backscatter are superimposed on (a) and (b). The vertical dashed line denotes the time of the most significant surface wind shift. The arrival of low cloud base is coincident with the wind shift, and the arrival of relatively large aerosol backscatter lags the wind shift by about 6 min.

(Fig. 15c) that lagged the most significant wind shift, reduction in T_d (Fig. 8b), and arrival of low cloud base. The enhanced backscatter was likely wind-blown dust lofted earlier by the vigorous gravity current flow behind the gust front. The enhanced low-level backscatter was capped by a layer of low backscatter centered near 500 m (annotated in Fig. 15c) by 0450 UTC. This minimum perhaps represents more pristine air that originated some distance to the west, as the altitude of this minimum corresponds to the residual gravity current feeder-flow jet shown in Fig. 14b.

(iii) Thermodynamics and cloud distribution

Analyses of θ and r_v derived from the MPR (Figs. 8a,b) provide the first ever detailed observations of in-

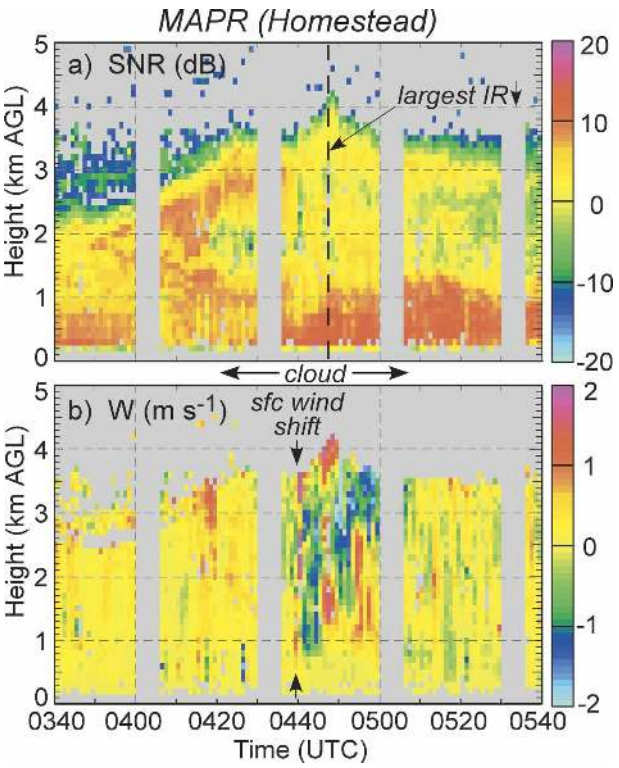

FIG. 16. Time vs height section of (a) SNR and (b) *W* from the vertical beam of the 915-MHz MAPR located at Homestead. The time resolution is 60 s. The period of cloud cover is based on an increase in downwelling infrared radiation (IR↓). The largest IR↓, marked by the dashed line, represents the inferred lowest cloud base. The surface wind shift is indicated by the arrows in (b).

ternal bore thermodynamics. The isentropes between 1.5 and 3.5 km AGL exhibit initial ascent around 0245 UTC and then an increasing slope starting near 0345 UTC as the bore approached. Although their behavior is similar, the isohumes (constant r_v) within the 1.5–3.0-km layer exhibit an initial rise at a later time (0330 UTC). The upward excursion of the 310-K isentrope and 9 g kg^{-1} isohume, both of which were within the NBL near 0.5 km at 0200 UTC, were both 1.6 km. A cold and moist perturbation was measured within the bore interior at 0435 UTC, implying ascent of stable NBL air. At 0200 UTC a layer of enhanced 915-MHz SNR near 1.5 km (indicative of the inversion and associated vertical gradient in r_v) displays a slow ascent that then accelerates upward near 0330 UTC, consistent with the behavior of the isentropes. Thus, all three surfaces—θ, r_v, and SNR—were displaced upward by maximum displacement heights (within the bore) of 1.6–1.9 km, respectively (Table 1). The 310-K isentrope and 9 g kg^{-1} isohume exhibited a negligible net displacement between 0200 and 0600 UTC. Differences among θ, r_v, and SNR can be attributed to the fact that θ and r_v are not conserved in saturated processes. The permanent displacement heights (H_{0600}–H_{0200}) of these surfaces (prior to the bore perturbation at 0200 UTC to post bore conditions at 0600 UTC) were 0.6–0.9 km. The maximum displacement heights exceed values of about 1 km calculated in another bore analyzed by Koch and Clark (1999) and are relevant to convective initiation (CI). In this case minor CI was observed as late as 0420 UTC south of S-Pol at the location marked "cell" in Fig. 14a.

Although the 7 g kg^{-1} isohume surface ascended during bore passage, a net drying below 1.5 km AGL was recorded by the MPR (Fig. 8b). This is attributed to advection of dry gravity current air in the westerly flow behind the CBZ and is consistent with the gravity current feeder jet and decrease in aerosol backscatter near 500 m AGL. Despite this low-level drying, the precipitable water (PW) after bore passage was about 2 mm (8%) higher than before due to upward transport of water vapor within the bore.

A cloud band that accompanied the bore passage over the MIPS is represented by increases in PW, integrated cloud water (ICW) and infrared (IR) temperature shown in Figs. 7c,d. The 28-km width of the cloud band was determined by the ceilometer (Fig. 15c), using the cloud duration of 40 min and movement speed of 11.5 m s^{-1}. This value is comparable to the width (25–30 km) determined from the S-Pol −12 dB*Z* outer contour at 0332 UTC (Fig. 13a). The cloud base at the leading edge gradually descended from 2.2 km initially to 1.9 km at 0428 UTC and then dropped rapidly to a minimum base of 1.4 km within the core during the 0429–0435 UTC period. After 0435 UTC the cloud base ascended monotonically to a maximum level of 3.3 km near the trailing edge at 0452 UTC. With the exception of a uniform cloud base within the core region, undulations are suggested in ceilometer patterns[5] before and after core passage. The cloud top is likely represented by the 915-MHz backscatter. The MAPR SNR (Fig. 16a) shows an inferred maximum cloud top of 4.1 km AGL around 0456 UTC. This value is consistent with S-Pol *Z* measurements that revealed cloud top heights near 4 km around this time. Extinction of the ceilometer signal within the cloud is inversely proportional to the vertical depth of the white shaded region in Fig. 15c. The cloud water path (extinction) is relatively large in advance of and at the location of lowest cloud base

[5] The effective horizontal resolution is the temporal resolution (15 s) multiplied by the advection speed (11.5 m s^{-1}), or 170 m.

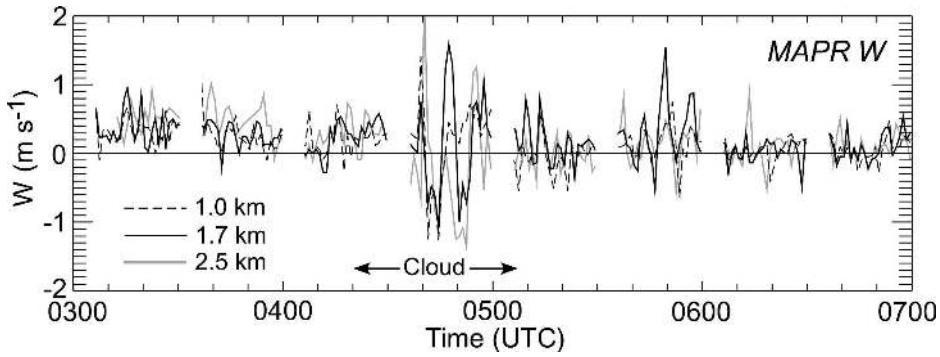

FIG. 17. Time series of W derived from the MAPR at the 1.0, 1.7, and 2.5 km AGL levels.

(0420–0435 UTC), and relatively small in the turbulent trailing portion of this cloud band.

The variation in cloud base implies a range of initial parcel heights and associated thermodynamics. Two contrasting parcel paths are shown in Fig. 10. The minimum cloud base of 1.4 km implies a parcel origin in the stable NBL near 200 m AGL. This parcel would have experienced appreciable negative buoyancy over a 2.5-km-deep layer up to its LFC near 3.3 km. This picture is consistent with the MPR θ field (Fig. 8a) in which θ is nearly constant between 200–300 m AGL up to near 1.5 km. The 6-K increase in θ between 1.5 and 3.1 km is consistent with saturated adiabatic ascent. A maximum buoyancy parcel would have originated just above the NBL within the residual layer near 0.9 km AGL. The LCL of this parcel (1.9 km) is consistent with the ceilometer cloud base height in advance of the bore wind shift.

The MPR also provides measurements of ICW that clarify inferences on cloud properties. The ICW peaked at 6.4 mm at 0435 UTC (Fig. 7c).[6] The maximum cloud depth of 2.7 km was estimated from the ceilometer-measured cloud base height of 1.4 km AGL and a cloud top of 4.1 km indicated by the MAPR. Using the observed cloud base temperature of 290 K, the adiabatic LWC is estimated to be 2.5 g m^{-3} (near cloud top) with a corresponding ICW of 6.7 mm, which is close to the observed value of 6.4 mm. Thus, the cloud exhibited a LWC that was about 95% of the adiabatic value.

[6] Koch and Clark (1999) noted an ICW value of about 10 mm from a two-channel microwave radiometer as a bore passed over the site. This implies a deeper cloud, and indeed, convective initiation was occurring around this time.

3) KINEMATICS OF THE BORE CORE

The relative airflow in Fig. 13 reveals well-defined low-level convergence and updraft at the leading edge of the CBZ core at 0332 and 0519 UTC. Additional details on the structure of the CBZ core were measured by the 915 and MAPR. The bore core passed over the MIPS at 0429–0450 UTC and over the MAPR at 0439–0500 UTC. Both profilers measured variable W (± 2 m s^{-1}) and high spectral width values within the 1.5–3.5 km AGL layer of the core (the portion of the bore with the deepest cloud) and the trailing cloud. The leading edge of the core region exhibited a deep and narrow (~1–2 min duration, ~1 km in width) updraft measured by the MAPR at 0440 UTC. Both profilers sampled a longer duration (4–5 min, 3-km width, 2–3 km deep) downdraft of about 1 m s^{-1} magnitude that trailed the leading updraft. Subsequent updraft/downdraft struc-

TABLE 1. Heights and displacements of specific isolines of radiometer retrieved/derived quantities (θ and r_v) and 915-MHz profiler SNR constant surfaces before, during, and after bore passage over the MIPS.

	Height (km AGL)			Displacement (km)	
Parameter	0200 UTC	Maximum	0600 UTC	Maximum	$H_{0600} - H_{0200}$
$\theta = 314$ K	1.9	3.1	2.5	1.2	0.6
$\theta = 310$ K	0.5	2.1	0.7	1.6	0.2
$r_v = 7$ g kg^{-1}	1.7	2.7	2.3	1.1	0.6
$r_v = 9$ g kg^{-1}	0.6	2.2	0.4	1.6	−0.1
MIPS 915 SNR (−10 dB)	1.6	>3.5	2.5	>1.9	0.9
MAPR 915 SNR (0 dB)	1.8	4.1	2.8	2.3	1.0

tures were limited in vertical extent to 1–2 km. Updraft values below 1 km (within the most stable air) were <1 m s^{-1} at both sites. The maximum and most sustained updraft was measured by the MAPR above 3.5 km between 0443 and 0447 UTC. According to parcel analysis (Fig. 10) this updraft was likely buoyant above the estimated LFC.

c. Bore weakening and the solitary wave stage

By 0519 UTC, the CBZ updraft maximum value near $x = 45$ km had decreased to 1.6 m s^{-1} at the 0.25 km AGL level (Fig. 13b). As noted in section 6b(1), a second low-amplitude wave (solitary wave 2) marked by weak updraft and a modest increase in Z above 1.5 km AGL is apparent near $x = 60$ km.[7] Each wave was accompanied by a distinct cloud band about 20 km wide, separated by a relative minimum in Z immediately in advance of the primary (trailing) updraft (see Figs. 13b and 14c,d). The band identified as 2 corresponds to the weak solitary wave that formed within the elevated inversion located near 2 km AGL [see section 6b(2)i and Fig. 14]. The relative flow at low levels is front to rear (FTR) throughout the domain. The FTR flow within wave 1, combined with the absence of thermodynamic (and wind direction) changes at the SLAP surface station (Fig. 6d) located at $x = 46$ km, corroborates that the bore had transformed to a solitary wave propagating along the surface-based inversion by 0519 UTC (see also Fig. 1c). Thus, two solitary waves were present by 0519 UTC: (i) the trailing solitary wave connected to the surface-based inversion was the remnant of the long-lived bore and (ii) the leading wave formed near 0415 UTC and propagated within the elevated inversion.

Examination of surface data at Gage, Oklahoma, about 30 km east-southeast of SLAP, showed one primary pressure crest (~1 mb amplitude) centered near 0515 UTC. By extrapolation, this wave is interpreted as a continuation of the easternmost disturbance (2) that was amplifying within the elevated inversion during its passage over SLAP at 0435 UTC (Fig. 6d). The estimated propagation speed is 18 m s^{-1}. The NBL was even more stable at Gage, where the surface T was about 22°C at the time of passage. Based on estimated values of the surface-based inversion ($h_0 = 800$ m, $\Delta\theta_v = 5$ K), the gravity wave propagation speed (c_{gw}) is computed at 11.6 m s^{-1} using the relation (Simpson 1997)

$$c_{gw} = \left[g\left(\frac{\Delta\theta_v}{\theta_v}\right) h_0 \right]^{1/2}, \tag{1}$$

where $\Delta\theta_v$ is the difference in average θ_v across the inversion. The phase speed determined from estimated parameters of the elevated inversion ($\Delta\theta_v = 8$ K, $\Delta z = 500$ m; refer to Fig. 4b) is also about 12 m s^{-1}. The disparity between the observed and linear theory may be related to nonlinear effects that become important for larger amplitude gravity waves (Christie 1989).

7. Discussion

The comprehensive measurements of the evolving CBZ and NBL in this case have disclosed several properties that warrant comparison with theory and other observations.

a. Comparison with theory

1) Bore initiation

Surface measurements at the BOIS mesonet site (Fig. 6a) imply the existence of a bore during the developing NBL stage as early as 0130 UTC, before astronomical sunset. Bore generation by gravity currents is hypothesized to be dependent on the ratio of the stable NBL depth (h_0) to the gravity current depth (d_0). According to tank experiments conducted by Rottman and Simpson (1989), bore formation occurs when the ratio h_0/d_0 exceeds a value of about 0.25. An estimate for d_0 was obtained from surface data at 0130 UTC using the relation (Koch et al. 1991)

$$d_0 = \frac{\theta_{vc}\Delta p}{\rho_w g\left[\dfrac{p_c}{p_w}\,\theta_{vw} - \theta_{vc}\right]}, \tag{2}$$

where "c" and "w" subscripts denote values within the cold and warm air, respectively. All variables are standard, θ_v: virtual potential temperature, p: pressure, ρ: air density, and g: acceleration due to gravity. The difference $\theta_{vw} - \theta_{vc}$ (averaged over the depth d_0) is taken to be one-half the difference in surface values (assuming that this difference decreases linearly to zero at d_0). Substitution of surface values (Fig. 6a) yields a d_0 of about 1.5 km. The MIPS/RASS T_v measurements at 0130 UTC show that h_0 was about 0.3 km. The ratio, $h_0/d_0 = 0.3/1.5 = 0.2$, is in close agreement with the 0.25 threshold, given the observational uncertainties in h_0 (± 0.2 km) and d_0 (± 0.1 km). Ralph et al. (1993) also found that an estimated value of $h_0/d_0 = 0.2$ was sufficient to induce gravity waves adjacent to a gravity current (a scale-contracted cold front). Moreover, accord-

[7] The analyzed vertical motion and cloud field is consistent with the surface measurements from SLAP, which indicate convergent flow and pressure variations corresponding to the passage of each updraft.

ing to the numerical simulations of Liu and Moncrieff (2000), the low-level stability (N_{BV} = 0.011 s^{-1}, normalized to a 700 m depth) was sufficient for bore formation. These theoretical considerations support the inference (based on the significant increase in surface pressure ahead of the gust front) that an incipient bore had formed within the 0130–0330 UTC time frame.

Several previous studies have examined bore formation early in the NBL period, including Simpson et al. (1977) for a bore produced by a shallow sea breeze front one hour before sunset; Koch et al. (1991) for bore development between 0200 and 0600 UTC (Pennsylvania–Maryland), and Koch and Clark (1999) for a bore observed between 0200 and 0400 UTC (Oklahoma). These studies lacked high temporal resolution soundings within the NBL. In the present study, we have utilized frequent low-level soundings (as provided by the RASS and MPR) to improve interpretation of wave phenomena in a rapidly evolving NBL environment.

2) BORE STRENGTH

The bore strength is defined by the ratio h_1/h_0, where the mean bore depth h_1 may be highly variable in space/time. Estimates of h_1 can be determined from soundings or measurements of airflow within and around the bore (e.g., Rottman and Simpson 1989; Koch and Clark 1999). A kinematic estimate of h_1 was derived from the vertical jump in the front-to-rear airflow patterns in Fig. 13a. This figure reveals air rising from the NBL to the 2.4–4.0 km AGL layer. We conservatively estimate h_1 to be the midpoint of this layer, or 3.2 km. With an NBL depth (h_0) of 0.7 km, the bore strength is $h_1/h_0 = (3.2 \pm 0.2)/(0.7 \pm 0.1) = 4.5$ (range of 3.8 to 5.7), which makes this bore that the strongest documented bore case. In comparison, Koch et al. (1991) determined a bore strength of 3.3 for a strong bore having a depth h_1 of 2.3 km.

Two-layer hydraulic theory can also be used to estimate bore strength and categorize bore disturbances according to the relative depths of the gravity current (d_0) and nocturnal inversion (h_0), in the form of the ratio d_0/h_0 versus Froude number (Fr). The latter is defined as the ratio of propagation speed of the gravity current c_{gc} to the phase speed of an internal gravity wave c_{gw} confined to the surface-based stable layer (e.g., Fr = c_{gc}/c_{gw}; see Rottman and Simpson 1989; Koch et al. 1991). The values of c_{gw} and c_{gc} were determined from Eq. (1) and the relation (Wakimoto 1982)

$$c_{gc} = \mathrm{Fr}\left(\frac{\Delta p}{\rho_w}\right)^{1/2}, \tag{3}$$

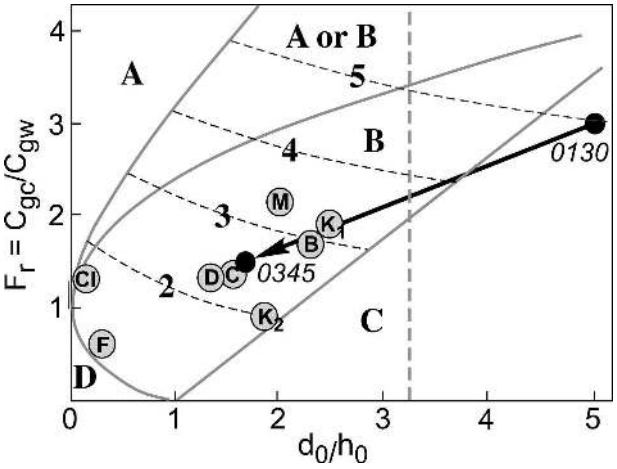

FIG. 18. Bore strength h_1/h_0 (dashed lines) and classification boundaries [solid gray curves, determined from hydraulic theory of Rottman and Simpson (1989)] as a function of Froude number (Fr) and the ratio of gravity current to stable layer depth (d_0/h_0). The bore depth is defined by h_1. The black-filled circles connected by the thick gray arrow denote the change in bore/NBL parameters during the early stages of the bore discussed in this paper. Circled letters refer to the same parameters for other selected observational studies: Cl: Clarke et al. (1981), F: Fulton et al. (1990), C: Carbone et al. (1990), K_1: Koch et al. (1991), K_2: Koch and Clark (1999), and D: Demoz et al. (2005). The portion of the diagram to the right of the vertical dashed gray line represents an extrapolation of a figure adapted from Koch et al. (1991).

where Δp is the pressure variation from warm to cold air across the gravity current and ρ_w is the density in the warm air.

These ratios are plotted as solid black circles in Fig. 18 for two times representing the formative (0130 UTC) and early mature (0345 UTC) stages of the bore. For both times, h_0 and $\Delta\theta_v$ were determined from MIPS data, d_0 was determined from Eq. (2) (assuming the same NBL profiles exist at the bore location), and Δp and ($\theta_{vw} - \theta_{vc}$) were obtained from surface data. At 0130 UTC the ratios are $d_0/h_0 = 1.5/0.3 = 5$ and $c_{gc}/c_{gw} = 12.7/4.2 = 3.0$. These values place the bore classification within the Type C (blocked flow) category and the extrapolated bore strength at about 5. Notably, this is close to the bore strength of 4.5 determined from observed airflow. A bore strength value this high suggests that the disturbance will exhibit the appearance of a gravity current (Rottman and Simpson 1989), which was the case during the 0130–0330 UTC period. By 0345 UTC, the NBL inversion magnitude ($\Delta\theta_v$) and depth (h_0) had increased to 5°C and 0.7 km, and the gravity current parameters Δp and (θ_{vw}-θ_{vc}) (at GOOD; Fig. 6b) had decreased to 1.8 hPa and 5°C, producing decreases in the depth d_0 (to 1.2 km) and c_{gc} (to 11.8 m s^{-1}). In terms of d_0/h_0 versus Fr (Fig. 18), the point

has shifted well to the left, and the bore strength is now 2.5, placing its classification within the Type B (partially blocked) category. Thus, the hydraulic theory appears to react in a very sensitive manner to the observed changes in coupled NBL and gravity current properties.

In laboratory simulations (Rottman and Simpson 1989) the bore strength (h_1/h_0) differentiates laminar (undular) bores having $h_1/h_0 < 2.0$ from turbulent bores where $h_1/h_0 > 3.0$. In turbulent laboratory bores, the turbulence is produced on the relative downwind (trailing) side via shear production. A similar structure is suggested in the present case. Figures 15 and 16 reveal a turbulent structure above 1.5 km AGL in the wake of the bore core (marked by the lowest cloud base). This layer exhibits appreciable vertical shear within the bore wake, shown in Fig. 13. Although a Richardson number (Ri) is difficult to estimate because of complexities in the initial temperature profile and total lifting, the value of Ri is likely small because a nearly constant θ layer, that was initially just above the capping inversion near 1.5 km AGL (Fig. 4), was likely present within 2.0–3.5-km layer (see Fig. 13b). Turbulence production was further complicated and likely enhanced (via buoyant production) by the presence of clouds, mixing, and associated latent heating.

This is the first documented case of turbulent flows within an atmospheric bore (to our knowledge), although Koch et al. (1991) inferred turbulence based on water vapor variability measured by a Raman lidar. It is noteworthy that Christie (1989) determined, through numerical integration of the Benjamin–Davis–Ono (BDO)–Burgers equation, that the hydraulic jump wave form of a bore tends to be preserved (i.e., trailing undular waves do not form) for bores with increased levels of turbulence (e.g., refer to Fig. 14 in Christie 1989).

Although weak bores are undular (Clarke et al. 1981; plotted as Cl in Fig. 18), multiple waves were also present in this case—at the long wavelength of about 20 km as well as at shorter wavelengths of 8–12 km (Fig. 14c). The latter wavelength $O(10\text{ km})$ is consistent with numerous observations and numerical model results. Simpson (1997) states that the wavelength predicted by hydraulic theory is related to the bore strength according to $\lambda \approx 10(h_1/h_0) = 30$ km. This value exceeds the observed wavelength (for waves 1, 1A, and 1B) by about a factor of 3, and does not apply to the 20-km wavelength between 1 and 2, because wave 2 formed on the elevated inversion.

3) CBZ propagation speed

Why did the CBZ propagation speed decrease from 16 m s^{-1} during the initial bore stage to 11 m s^{-1} during the latter solitary wave stage? The bore propagation speed can be related to bore strength according to a relation from hydraulic theory (Rottman and Simpson 1989),

$$c_{\text{bore}} = c_{\text{gw}}\left[\frac{1}{2}\frac{h_1}{h_0}\left(1 + \frac{h_1}{h_0}\right)\right]^{1/2}. \quad (4)$$

Inserting bore strength (h_1/h_0) and c_{gw} values obtained previously (5 at 0130 UTC and 2.5 at 0345 UTC) produces respective c_{bore} values of 16.3 and 16.9 m s^{-1}, which are very close to the observed CBZ propagation speed of 15.9 m s^{-1} around 0300 UTC. In contrast, the gravity current relation [Eq. (3)] produces about 12–13 m s^{-1} during this time period. We conclude that the observed CBZ propagation speed is consistent with that of a bore predicted by hydraulic theory.

Another relation for bore propagation speed developed by Crook and Miller (1985), $c_{\text{bore}} = (2N_{\text{BV}}h_1)/\pi$, yields a value of 22.9 m s^{-1}, which is about 7 m s^{-1} (44%) too high. Such a disparity may be related to the assumptions underlying this derivation, namely incompressible, energy conserving flow, which may not apply to the deeper (cloud filled) and more turbulent bore in the present case.

We now seek to explain the decrease in disturbance propagation speed around 0400 UTC. The gravity wave relation [Eq. (1)] predicts a propagation speed of 9.6 m s^{-1} with the parameters $h_0 = 800$ m and $\Delta\theta_v = 3.5$°C (7°C at the surface) derived from the SLAP mesonet site. Although this value is about 12% less than the observed value (10.8 m s^{-1}), it appears to explain the decrease in propagation speed of the CBZ during the 3-h period of observations as the CBZ evolved from an incipient bore to a solitary wave. Moreover, since the speed of nonlinear waves exceeds that for linear waves (Christie 1989), the observed speed is close to the theoretical prediction. Additional complications in the wave dynamics and propagation, not accounted for by the linear theory, include the nonlinear θ profile and the presence of latent heating over the 2.5-km-deep layer (Crook 1986).

4) Solitary wave generation ahead of the bore

Two aspects of wave formation are unusual in this case: (i) Wave 1B formed at the front edge of the main bore and then propagated at a greater speed ahead of the bore, despite having a lower (assumed) amplitude. (ii) Wave 2 also formed ahead of the bore on the elevated inversion, not the surface-based inversion.

The solitary wave labeled 2 in Figs. 13b and 14 formed near 0415 UTC about 25 km in advance of bore and initially moved at about 80% the bore speed. It is

hypothesized that this wave formed within the elevated inversion located near 2 km AGL (Figs. 4 and 10). Assuming an elevated inversion strength ($\Delta\theta_v$) of 5.0 K ($\pm$1.0 K) and an inversion depth (Δh_{inv}) of 500 m ($\pm$200 m) at the MIPS site, Eq. (1) yields a wave propagation speed of 8.9 m s^{-1} ($\pm$2.5 m s^{-1}), very close to the observed speed of 9.2 m s^{-1}. The elevated inversion strength increased toward the east (e.g., $\Delta\theta$ was about 8 K at DDC, Fig. 4b), so greater propagation speeds would be expected (e.g., 12.5 m s^{-1} from the DDC sounding).

It is further hypothesized that the bore initiated wave 2, perhaps through an increase in vertical wave propagation through the surface-based stable layer. A balloon sounding released from Homestead at 1027 UTC (4 h after bore passage) showed that the previous residual layer (of neutral static stability) was no longer present. The static stability between the NBL inversion top and the elevated stable layer was about $\Delta\theta/\Delta z = 3$ K km^{-1}, which was perhaps sufficient to promote vertical propagation of wave energy from the NBL inversion to the elevated stable layer. A better understanding of this process would require numerical simulations using realistic profiles of wind and thermodynamic quantities. The key observations of the NBL and bore/wave properties during this transition include the following: (i) The nocturnal boundary layer was becoming increasingly stable, as was the residual layer above it. (ii) The depth and potential temperature change across the elevated inversion increased in the direction (east) of wave propagation. (iii) The bore was weakening and transitioning to a surface-based solitary wave. (iv) A second solitary wave propagated along the elevated inversion, initially at a speed slower than that of the bore. (v) The propagation speed of the elevated solitary wave increased by a factor of 2 as the wave experienced a stronger and deeper elevated inversion. As this wave amplified, its propagation speed may have increased from nonlinear effects, given that solitary wave propagation speed is a function of wave amplitude (Christie 1989).

b. Comparison with previous studies

A variety of bores have been reported in the literature. A subset of these is plotted for comparison to the present case within Fr versus d_0/h_0 space in Fig. 18. Although these bores represent a wide range of conditions, most fall into the Type B (partially blocked) category, with bore strengths ranging from weak ($\sim$1) to strong ($>$3). The bore in the present case is one of the strongest documented, and is the only Type C bore in this limited sample.

1) THERMODYNAMICS AND KINEMATICS

Surface pressure increases of 1–2 hPa are typical for bores (Menhofer et al. 1997). Pressure increases exceeding 5 hPa have been documented (Fulton et al. 1990). The lag in arrival of drier air (following the wind shift) in the present case appears to be common for bores initiated by gravity currents. A similar behavior is documented by Fulton et al. (1990) and Koch and Clark (1999). Vertical motion (w) magnitudes of 2–5 m s^{-1} in the present case are similar to w values measured in several other cases (Clarke et al. 1981). In the present case, the maximum w (w_{max}) decreased as the NBL stability and depth increased, which would lead to a reduction in bore strength. During the incipient strong bore stage, w_{max} was $\sim$5 m s^{-1}; as the bore evolved to a solitary wave, w_{max} decreased to about 2 m s^{-1}.

Two-dimensional flow fields within the plane normal to the bore major axis have been rarely documented with observations. The present case resembles the analysis presented by Koch and Clark (1999) in several respects. The bore disturbance was wide in each case (20–30 km), and the resolvable flow within the bore exhibited a similar front-to-rear flow (jump updraft) representing the main branch of the bore hydraulic jump. Koch and Clark analyzed a mean updraft of 0.9 m s^{-1} (5-min average) within the bore core, but turbulent structures were not resolved in their analysis. The mesoscale ascent (on the order of tens of centimeters per second) in advance of the bore core has been implied in several cases, including Koch et al. (1991), Koch and Clark (1999), and the case herein.

2) CLOUD DISTRIBUTION

Detailed measurements of clouds associated with bores have been lacking in many previous studies. Cloud properties in several cases of weak bores and solitary waves have been documented with photography (Clarke et al. 1981; Haase and Smith 1984; Doviak and Ge 1984; Mahapatra et al. 1991; Wakimoto and Kingsmill 1995). Koch and Clark (1999) determined a relatively broad cloud field with a 23-km width based on radiometer-derived ICW. In this respect, their case (also a strong bore, plotted as K_1 in Fig. 18) is similar to the 25–30-km-wide cloud field in the present case. Demoz et al. (2005) also presented two-channel radiometer data from an undular bore passage, revealing two shallow cloud bands with widths of 4 and 6 km, and respective ICW values 0.3 and 1.3 mm. When compared to the 2–6-km width of cloud bands associated with weak bores (Clarke et al. 1981; Christie 1989; Demoz et al. 2005), it appears that strong bores generate deeper and wider cloud bands, with widths about one order of

magnitude greater and a more complex structure consisting of a smooth, lowered base (4 km wide) within the core region.

8. Summary and conclusions

The complete evolution of a gust front to bore to solitary wave transformation has been documented with radar and profiling instruments in this case. Interpretations of this transformation were supported by comprehensive thermodynamic and kinematic measurements of the NBL evolution. Figure 1 summarizes the evolution of this CBZ and serves as a reference supporting the following significant findings:

(i) The bore formed very early in the NBL cycle, when the NBL was about 300 m deep and exhibited modest static stability (surface cooling of 4°C from the maximum; N_{BV} about 0.011 s^{-1}). The NBL thermodynamic and wind profiles evolved continuously during the evolution of this system. An eventual solitary wave was associated with relatively strong static stability (N_{BV} about 0.018 s^{-1}), about 4 h after bore formation.

(ii) During its formative stages, the bore was classified as strong ($h_1/h_0 = 4.5$) and exhibited a kinematic structure similar to that of a gravity current. The early bore displayed a jump updraft of 4–5 m s^{-1} magnitude with front-to-rear flow within this circulation.

(iii) During the mature bore phase, a second major (solitary) wave formed within an elevated inversion 25 km in advance of the bore. This wave continued to propagate eastward after the precursor bore/solitary wave dissipated. Likewise, surface-based waves formed ~10 km both in advance of and behind the primary bore over limited segments (30–60 km) of the bore length after 0430 UTC. The observation of secondary waves forming in advance of an existing bore has not been previously documented.

(iv) The initial propagation speed is consistent with a bore propagation speed. As the NBL stabilized, the propagation speed decreased from 15 to 11 m s^{-1}, with the latter being consistent with the propagation of a gravity wave within the NBL.

(v) Strong deep updrafts within the core of the mature bore were absent as it passed over two wind profilers.

(vi) The core and trailing cloud field were turbulent, in accord with predictions from hydraulic theory for strong bores. In contrast, the cloud field in advance of the bore core was laminar, and a prolonged weak ascent (about 0.5 m s^{-1} for 1 h) preceded the core.

(vii) The bore cloud field was 25–30 km wide and up to 2.5 km deep (base to top). Saturation was attained by a combination of strong vertical motion within the convergent bore core superimposed on prolonged mesoscale ascent. Nearly adiabatic liquid water content and low cloud base (1.4 km AGL) were measured within the core, which was cold relative to the surroundings throughout much of its depth.

(viii) The bore produced a net addition (8%) of water vapor to the atmospheric column (despite drying below 1.5 km) due to a permanent 0.5–1.0-km displacement of air parcels above the residual gravity current level.

(ix) The maximum parcel excursion of about 2 km within the core was near the threshold for convective initiation.

A more thorough understanding of this case (and bore development/evolution within an evolving NBL in general) using numerical models (e.g., Crook and Miller 1985; Jin et al. 1996; Goler and Reeder 2004) will likely require an accurate portrayal of NBL evolution, representation of realistic θ profiles in the NBL (e.g., a height dependent N_{BV}), and knowledge of heterogeneities in NBL properties (wind, stability) that were measured or implied in this case.

Acknowledgments. Sincere thanks are extended to Justin Walters and Haldun Karan for programming and data analysis assistance, and to all IHOP investigators whose collaborative spirit and dedicated efforts made the IHOP field campaign a success. Comments by Timothy A. Coleman, Dr. Andrew Crook, and two anonymous reviewers significantly improved the manuscript. This material is based upon work supported by the National Science Foundation under Grants ATM-0002252 and ATM-0130611.

REFERENCES

Carbone, R. E., J. W. Conway, N. A. Crook, and M. W. Moncrieff, 1990: The generation and propagation of a nocturnal squall line. Part I: Observations and implications for mesoscale predictability. *Mon. Wea. Rev.,* **118,** 26–49.

Cheung, T. K., and C. G. Little, 1990: Meteorological tower, microbarograph array, and sodar observations of solitary-like waves in the nocturnal boundary layer. *J. Atmos. Sci.,* **47,** 2516–2536.

Christie, D. R., 1989: Long nonlinear waves in the lower atmosphere. *J. Atmos. Sci.,* **46,** 1462–1491.

——, K. J. Muirhead, and A. L. Hales, 1978: On solitary waves in the atmosphere. *J. Atmos. Sci.,* **35,** 805–825.

Clarke, R. H., R. K. Smith, and D. G. Reid, 1981: The morning

glory of the Gulf of Carpentaria: An atmospheric undular bore. *Mon. Wea. Rev.,* **109,** 1726–1750.

Crook, N. A., 1986: The effect of ambient stratification and moisture on the motion of atmospheric undular bores. *J. Atmos. Sci.,* **43,** 171–181.

——, and M. J. Miller, 1985: A numerical and analytical study of atmospheric undular bores. *Quart. J. Roy. Meteor. Soc.,* **111,** 225–242.

Demoz, B. B., and Coauthors, 2005: The cold front of 15 April 1994 over the central United States. Part I: Observations. *Mon. Wea. Rev.,* **133,** 1525–1543.

Doviak, R. J., and R. Ge, 1984: An atmospheric solitary gust observed with a Doppler radar, a tall tower and a surface network. *J. Atmos. Sci.,* **41,** 2559–2573.

——, S. S. Chen, and D. R. Christie, 1991: A thunderstorm-generated solitary wave observation compared with theory for nonlinear waves in a sheared atmosphere. *J. Atmos. Sci.,* **48,** 87–111.

Droegemeier, K. K., and R. B. Wilhelmson, 1987: Numerical simulation of thunderstorm outflow dynamics. Part I: Outflow sensitivity experiments and turbulence dynamics. *J. Atmos. Sci.,* **44,** 1180–1210.

Fabry, F., 2004: Meteorological value of ground target measurements by radar. *J. Atmos. Oceanic Technol.,* **21,** 560–573.

Fulton, R., D. S. Zrnić, and R. J. Doviak, 1990: Initiation of a solitary wave family in the demise of a nocturnal thunderstorm density current. *J. Atmos. Sci.,* **47,** 319–337.

Goff, R. C., 1976: Vertical structure of thunderstorm outflows. *Mon. Wea. Rev.,* **104,** 1429–1440.

Goler, R. A., and M. J. Reeder, 2004: The generation of the morning glory. *J. Atmos. Sci.,* **61,** 1360–1376.

Güldner, J., and D. Spänkuch, 2001: Remote sensing of the thermodynamic state of the atmospheric boundary layer by ground-based microwave radiometry. *J. Atmos. Oceanic Technol.,* **18,** 925–933.

Haase, S. P., and R. K. Smith, 1984: Morning glory wave clouds in Oklahoma: A case study. *Mon. Wea. Rev.,* **112,** 2078–2089.

Jin, Y., S. E. Koch, Y.-L. Lin, F. M. Ralph, and C. Chen, 1996: Numerical simulations of an observed gravity current and gravity waves in an environment characterized by complex stratification and shear. *J. Atmos. Sci.,* **53,** 3570–3588.

Karan, H., and K. R. Knupp, 2006: Mobile integrated profiler system (MIPS) observations of low-level convergent boundaries during IHOP. *Mon. Wea. Rev.,* **134,** 92–112.

Kingsmill, D. E., and N. A. Crook, 2003: An observational study of atmospheric bore formation from colliding density currents. *Mon. Wea. Rev.,* **131,** 2985–3002.

Koch, S. E., and W. L. Clark, 1999: A nonclassical cold front observed during COPS-91: Frontal structure and the process of severe storm initiation. *J. Atmos. Sci.,* **56,** 2862–2890.

——, P. B. Dorian, R. Ferrare, S. H. Melfi, W. C. Skillman, and D. Whiteman, 1991: Structure of an internal bore and dissipating gravity current as revealed by Raman lidar. *Mon. Wea. Rev.,* **119,** 857–887.

Liu, C., and M. W. Moncrieff, 2000: Simulated density currents in idealized stratified environments. *Mon. Wea. Rev.,* **128,** 1420–1437.

Mahapatra, P. R., R. J. Doviak, and D. S. Zrnic, 1991: Multisensor observation of an atmospheric undular bore. *Bull. Amer. Meteor. Soc.,* **72,** 1468–1480.

Menhofer, A., R. K. Smith, M. J. Reeder, and D. R. Christie, 1997: "Morning-Glory" disturbances and the environment in which they propagate. *J. Atmos. Sci.,* **54,** 1712–1725.

Ralph, F. M., C. Mazaudier, M. Crochet, and S. V. Venkateswaran, 1993: Doppler sodar and radar wind-profiler observations of gravity-wave activity associated with a gravity current. *Mon. Wea. Rev.,* **121,** 444–463.

——, P. J. Neiman, P. O. G. Persson, J. M. Bane, M. L. Cancillo, J. M. Wilczak, and W. Nuss, 2000: Kelvin waves and internal bores in the marine boundary layer inversion and their relationship to coastally trapped wind reversals. *Mon. Wea. Rev.,* **128,** 283–300.

Rottman, J. W., and J. E. Simpson, 1989: The formation of internal bores in the atmosphere: A laboratory model. *Quart. J. Roy. Meteor. Soc.,* **115,** 941–963.

Simpson, J. E., 1997: *Gravity Currents: In the Environment and the Laboratory.* 2d ed. Cambridge University Press, 244 pp.

——, D. A. Mansfield, and J. R. Milford, 1977: Inland penetration of sea-breeze fronts. *Quart. J. Roy. Meteor. Soc.,* **103,** 47–76.

Smith, R. K., 1988: Traveling waves and bores in the lower atmosphere: The "morning glory" and related phenomena. *Earth-Sci. Rev.,* **25,** 267–290.

——, and J. A. Noonan, 1998: On the generation of low-level mesoscale convergence lines over northeastern Australia. *Mon. Wea. Rev.,* **126,** 167–185.

Solheim, F., J. R. Godwin, E. R. Westwater, Y. Han, S. J. Keihm, K. Marsh, and R. Ware, 1998: Radiometric profiling of temperature, water vapor and cloud liquid water using various inversion methods. *Radio Sci.,* **33,** 393–404.

Tepper, M., 1950: A proposed mechanism of squall lines: The pressure jump line. *J. Meteor.,* **7,** 21–29.

Wakimoto, R. M., 1982: The life cycle of thunderstorm gust fronts as viewed with Doppler radar and rawinsonde data. *Mon. Wea. Rev.,* **110,** 1060–1082.

——, and D. E. Kingsmill, 1995: Structure of an atmospheric undular bore generated from colliding boundaries during CaPE. *Mon. Wea. Rev.,* **123,** 1374–1393.

Weckwerth, T. M., and Coauthors, 2004: An overview of the International H_2O Project (IHOP_2002) and some preliminary highlights. *Bull. Amer. Meteor. Soc.,* **85,** 253–277.

——, C. R. Pettet, F. Fabry, S. Park, M. A. LeMone, and J. W. Wilson, 2005: Radar refractivity retrieval: Validation and application to short-term forecasting. *J. Appl. Meteor.,* **44,** 285–300.

Zrnić, D. S., and A. V. Ryzhkov, 1998: Observations of insects and birds with a polarimetric radar. *IEEE Trans. Geosci. Remote Sens.,* **36,** 661–668.